Reduction of spherical and chromatic aberration in axial-scanning optical systems with tunable lenses

JAMES A. STROTHER[*]

Dept. of Biology, Whitney Laboratory for Marine Bioscience, University of Florida, FL 32080, USA
[*]*james.strother@whitney.ufl.edu*

Abstract: Optical systems with integrated tunable lenses allow for rapid axial-scanning without mechanical translation of the components. However, changing the power of the tunable lens typically upsets aberration balancing across the system, introducing spherical and chromatic aberrations that limit the usable axial range. This study develops an analytical approximation for the tuning-induced spherical and axial chromatic aberration of a general optical system containing a tunable lens element. The resulting model indicates that systems can be simultaneously corrected for both tuning-induced spherical and chromatic aberrations by controlling the lateral magnification, coma, and pupil lateral color prior to the tunable surface. These insights are then used to design a realizable axial-scanning microscope system with a high numerical aperture and diffraction-limited performance over a wide field of view and deep axial range.

1. Introduction

Biomedical research has been transformed by 3D optical microscopy techniques, including confocal [1,2], two-photon [3], and light-sheet microscopy [4,5]. In most circumstances, 3D information is obtained by capturing a sequence of images in the xy-plane while translating the optical system along the z-axis. Translation in the z-direction may be achieved using either traditional leadscrew actuators or faster piezoelectric actuators (e.g., Physik Instrumente P-725 or Thorlabs PFM450E). However, it is unclear if this approach may be used to achieve higher z-scanning speeds, as it requires accelerating the relatively large moving mass of the microscope objective. In addition, when used with fragile biological samples and liquid immersion objectives, the z-scanning speed must frequently be further limited to avoid sample movement and damage.

Multiple approaches have been explored for accelerating volumetric imaging, including varifocal lenses [6–14], remote focusing [15,16], extended depth of field microscopy [17,18], tomography [19], and holographic microscopy [20]. Varifocal lenses are relatively simple and compatible with common imaging modalities, making them an especially promising approach for performing fast z-scanning. Most commonly, a varifocal lens is positioned either directly behind the microscope objective or at a pupil located within the microscope body, and changes in the lens power produce rapid movement of the focal plane while maintaining the microscope objective in a fixed position. Numerous approaches have been explored for producing varifocal lenses, including elastic membrane based lenses [21], dielectric or electro-wetting lenses [22–24], liquid crystal lenses [25], electro-optic lenses [26], acoustic gradient index lenses [27,28], deformable mirrors [29,30], and others [31]. Although the specific properties of each technology vary, liquid-based varifocal elements are often capable of larger changes in lens power over milliseconds, while electro-optic and acoustic elements typically provide smaller lens power ranges over microseconds.

Although varifocal lenses enable rapid z-scanning, tuning-induced spherical aberration has been a major challenge in integrating these elements into microscopy systems. Modern microscope objectives are capable of imaging large fields of view at high numerical aperture with diffraction

limited performance. However, displacement of the focal plane from the design position introduces substantial amounts of uncorrected spherical aberration [32–35]. In many cases, the usable focal shift range is much smaller than that available with traditional z-translation methods. Prior studies have found that these tuning-induced aberrations may be reduced by using additional dynamic elements, including deformable mirrors [36,37] and multiple tunable lenses [34,38–42]. In addition, recent studies have demonstrated that liquid-based lenses with aspherical surfaces [43–52] or multi-configuration numerical optimization [53–55] can be used to reduce these aberrations. Even with recent advances, currently available methods typically require sacrifices in xy field of view, decreases in z scanning range, reductions in numerical aperture, or mechanically-complex tunable elements.

This study examines the aberrations produced by tunable elements with the aim of developing improved mitigation strategies. Approaches for correcting lateral color and magnification color are first discussed, and the effects of focal shifts on the wavefront aberration function at the entrance pupil are reviewed. Although the wavefront function at the entrance pupil provides qualitative insights into the problem, a precise mitigation strategy requires an understanding of the wavefront function at the exit pupil adjacent to the tunable lens surface, which is less easily obtained. To address this need, an analytical model is developed for the wavefront function at the exit pupil for on-axis points to a third-order approximation of ray height and a first-order approximation of focal shift. Importantly, this model is valid for all axisymmetric optical systems, even those that do not form perfect images in the initial configuration. Next, the obtained wavefront function and analytical ray tracing are used to construct an analytical model for the tuning-induced spherical aberration of a complete optical system containing a tunable lens surface. This model reveals the general conditions under which the first-order tuning-induced spherical aberration is eliminated. Surprisingly, it is found that the aberration may be removed by controlling the system magnification and coma at the tunable lens, and this correction does not require additional dynamic elements or aspherical surfaces. Next, a paraxial approximation is used to determine the general conditions necessary to eliminate tuning-induced axial chromatic aberration. The predictions of the analytical models are then verified using numerical ray tracing and realizable test cases. Finally, these constraints are used to design a wide field of view (550 μm), large focal shift (350 μm), large numerical aperture (NA=0.8), apochromatic (450-625μm) microscope system with diffraction-limited performance across the entire operating range. As designed, this system provides approximately an order of magnitude improvement in the diffraction-limited focus range when compared to traditional tunable lens designs.

2. Conditions for elimination of lateral color and magnification changes

For an axial-scanning system to operate effectively over long focus ranges, it is necessary to eliminate tuning-induced lateral color. This is readily achieved by positioning the tunable surface at a system pupil. Since the chief ray for an off-axis point (dashed grey line in Fig. 1(C)) intersects the optical axis at the pupil, a thin lens positioned at this location does not alter the trajectory of the chief ray. Consequently, if a tunable element is positioned at a system pupil that images to the entrance pupil without axial chromatic aberration, then wavelength-dependent changes in the power of the tunable element do not alter the lateral color. As it is very desirable to hold the lateral color fixed, subsequent analysis will assume that the tunable element is positioned at a system pupil corrected for axial color.

Following similar reasoning, when the tunable element is positioned at a system pupil, changes in the power of the tunable element displace the object space focal point along a trajectory that follows the chief rays. As has been previously discussed [8,56], the resulting change in
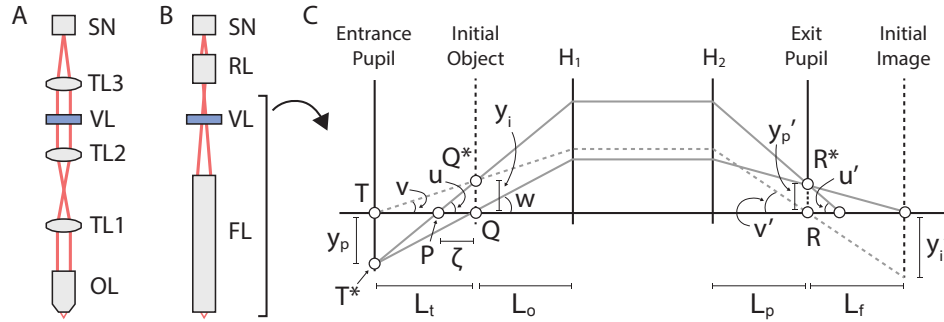
Fig. 1. (A) Schematic diagram of a typical axial-scanning optical system, in which a varifocal lens is positioned at an infinity-focused pupil formed by tube lenses (OL: objective lens, TL1-3: tube lenses, VL: varifocal lens, SN: sensor). (B) Schematic diagram of the generalized axial-scanning optical system examined in this study, in which components are represented by abstract thick lenses and light is not necessarily infinity-focused at the varifocal lens (FL: front lens, RL: rear lens, bracket indicates region shown in detail in C). (C) Detailed diagram of the system examined in this study, indicating the quantities used for developing analytical approximations.

magnification is given by

$$\frac{\mathrm{d}M}{\mathrm{d}\zeta} = \frac{M}{L_t},\tag{1}$$

where M is the paraxial lateral magnification of the optical system, ζ is the displacement of the focal position in a direction away from the lens, and L_t is the distance from the object to the entrance pupil. Consequently, the lateral magnification is constant when L_t approaches infinity, or equivalently when the system is telecentric in the object space or the chief ray angle (v) approaches zero.

3. Conditions for elimination of tuning-induced spherical aberration

3.1. Wavefront aberration function at the entrance pupil

As a first step towards developing an improved correction strategy, the effects of a shift in the object focal plane on the wavefront at the entrance pupil are calculated. To facilitate the derivation of simple equations appropriate for design purposes, this analysis will focus on the aberrations of ray pencils originating from on-axis positions. In this case, the change in the wavefront aberration function induced by a focal shift ζ as calculated for a flat reference surface located at the entrance pupil is

$$\delta W_e = (\lfloor PT^* \rfloor - \lfloor PT \rfloor) - (\lfloor QT^* \rfloor - \lfloor QT \rfloor),\tag{2}$$

where P is a point displaced from the focal plane by ζ along the optical axis, Q is the on-axis point within the initial focal plane, T is the on-axis point within the entrance pupil, T^* is the position of the intersection of a marginal ray from point P with the entrance pupil, and $\lfloor \ \rfloor$ denotes the optical path length between two points (see Fig. 1(C)). Although the wavefront aberration is often calculated for a spherical reference surface centered on the focal point, the wavefront function is well-defined for any reference surface and a flat surface is used here as it simplifies

the subsequent interpretation. Examination of the geometry allows Eq. (2) to be expanded as

$$\delta W_e = n_o L_t \left[1 - \zeta/L_t - \sqrt{(1 - \zeta/L_t)^2 + \tan^2 w} \right]$$
$$- n_o L_t \left(1 - \sqrt{1 + \tan^2 w} \right),$$

(3)

where n_o is the refractive index of the media at the object, and w is the angle of the marginal ray at the initial focal position.

3.2. Form of wavefront aberration function at the exit pupil

Although the wavefront aberration function at the entrance pupil provides some qualitative insights into the sources of focal shift induced aberrations, a quantitative understanding requires computation of the wavefront function at the exit pupil in front of the tunable lens surface. If the optical system perfectly images the entrance pupil to the exit pupil, then the optical path length is identical for all rays originating from a point on the entrance pupil and impinging on the corresponding point on the exit pupil. Consequently, the wavefront aberration function on the exit pupil is equal to the wavefront function evaluated at the corresponding points on the entrance pupil. However, real optical systems are rarely designed to produce sharp images in the pupil image space. In addition, it will later be shown that the deliberate inclusion of aberrations in the initial configuration can in fact be used to correct for the tuning-induced aberrations. For these reasons, it is necessary to understand the effects of focal shift on the wavefront aberration at the exit pupil for an imperfect optical system.

For an optical system with arbitrary aberrations, a focal shift ζ produces a change in the wavefront aberration function at the exit pupil for an on-axis position equal to

$$\delta W_x = (\lfloor PQ^*R^* \rfloor - \lfloor PQR \rfloor) - (\lfloor QR^* \rfloor - \lfloor QR \rfloor),$$

(4)

where Q^* is the position of the intersection of a marginal ray from P with the initial focal plane, R is the on-axis point within the exit pupil, and R^* is the position of the intersection of a marginal ray with the exit pupil plane (see Fig. 1(C)). Throughout the subsequent derivation, the focus shift ζ and the position at which the marginal ray intercepts the exit pupil y_p' are taken as variables while other system properties (e.g., L_f, L_p) are taken as fixed parameters. The variables ζ and y_p' are independent by construction, as they completely and uniquely describe the marginal ray being examined.

The term $\lfloor PQ^*R^* \rfloor$ in the above relationship may be expanded and calculated as

$$\lfloor PQ^*R^* \rfloor = \lfloor PQ^* \rfloor + \lfloor Q^*R^* \rfloor$$

(5)

$$\lfloor PQ^* \rfloor = n_o \zeta \sqrt{1 + \tan^2[u(\zeta, y_p')]}$$

(6)

$$\lfloor Q^*R^* \rfloor = \lfloor Q^*R \rfloor + \eta^*(\zeta, y_p'),$$

(7)

where $u(\zeta, y_p')$ is the angle between a marginal ray and the optical axis at the sample, and $\eta^*(\zeta, y_p')$ is equal to the optical path difference (OPD) between a marginal ray and the chief ray for an off-axis position on the initial focal plane (point Q^*). Similarly, the path length for a ray starting at the displaced focal point and running along the optical axis is equal to

$$\lfloor PQR \rfloor = n_o \zeta + \lfloor QR \rfloor.$$

(8)

The optical path length for a marginal ray emerging from the on-axis point Q is equal to

$$\lfloor QR^* \rfloor = \lfloor QR \rfloor + \eta(\zeta, y_p'),$$

(9)

where $\eta(\zeta, y_p')$ is equal to the OPD between a marginal ray and the chief ray for an on-axis position on the initial focal plane.

Further simplification requires elimination of the term $\lfloor Q^*R \rfloor$ from the above equations, which may be achieved by examining the conjugate system and assuming that the focal shift is infinitesimal. The optical path length of a ray emerging from a point at the center of the entrance pupil, passing through the point Q^*, and impinging on a point at the center of the exit pupil may be calculated as

$$\lfloor TQ^*R \rfloor = \lfloor TQ^* \rfloor + \lfloor Q^*R \rfloor, \tag{10}$$

where the first term may be expanded as

$$\lfloor TQ^* \rfloor = n_o L_t \sqrt{1 + (\zeta/L_t)^2 \tan^2[u(\zeta, y_p')]}. \tag{11}$$

The path length for a ray passing along the optical axis may also be calculated as

$$\lfloor TQR \rfloor = n_o L_t + \lfloor QR \rfloor. \tag{12}$$

If it is assumed that ζ is infinitesimal, the angle v between the ray $\overline{TQ^*}$ and the optical axis may also be assumed to be infinitesimal. As any in-focus system produces perfect images in the paraxial approximation, then it follows that the optical path length is constant for all rays in a pencil originating at point T on the entrance pupil and terminating at point R on the exit pupil, such that

$$\lfloor TQ^*R \rfloor = \lfloor TQR \rfloor. \tag{13}$$

The validity of the paraxial approximation in this specific context results from the assumption of infinitesimal ζ, but this does not reduce the overall system of equations to a paraxial approximation or otherwise impose any constraints on the aberrations present within the optical system.

Rearrangement of Eqs. (4)–(13) provides the change in the wavefront aberration function induced by a focal shift ζ of an on-axis position at the exit pupil

$$
\begin{aligned}
\delta W_x = \ & n_o \zeta \left(\sqrt{1 + \tan^2[u(\zeta, y_{p}')]} - 1 \right) \\
& - n_o L_t \left(\sqrt{1 + (\zeta/L_t)^2 \tan^2[u(\zeta, y_{p}')]} - 1 \right) \\
& + \eta^*(\zeta, y_{p}') - \eta(\zeta, y_{p}').
\end{aligned}
\tag{14}
$$

3.3. Contribution of η^* and η to the wavefront function at the exit pupil

The η^* and η terms of Eq. (14) represent the OPD between the marginal and chief ray at the exit pupil for off-axis and on-axis positions on the initial focal plane, respectively. Since the off-axis position is given by the intersection of the chief ray emanating from the focally-shifted position P with the original focal plane, these terms are still dependent on the focal shift. However, these terms are otherwise entirely defined by the optical properties of the system in its initial configuration. If the wavefront at the exit pupil is represented as the sum of a spherical wave and third-order aberrations, then η^* may be approximated as

$$
\begin{aligned}
\eta^*(\zeta, y_{p}') = \ & -n_f L_f \left(\sqrt{1 + \left[y_{p}'/L_f - y_i'(\zeta, y_{p}')/L_f\right]^2} - \sqrt{1 + \left[y_i'(\zeta, y_{p}')/L_f\right]^2} \right) \\
& + W_{040} \left[(x_{p}')^2 + (y_{p}')^2\right]^2 + W_{131}\, y_{p}'\, y_i'(\zeta, y_{p}') \left[(x_{p}')^2 + (y_{p}')^2\right] \\
& + W_{222}\, (y_{p}')^2 \left[y_i'(\zeta, y_{p}')\right]^2,
\end{aligned}
\tag{15}
$$

where n_f is the refractive index of the media in front of the tunable lens, L_f is the distance from the exit pupil to the image plane in the initial configuration, $y_i'(\zeta, y_{p}')$ is the image height for a pencil originating from point Q^*, and x_{p}' and y_{p}' are coordinates on the exit pupil. The terms

W_{040}, W_{131}, and W_{222} represent the spherical aberration, coma, and astigmatism of the initial configuration, respectively. Since only on-axis points are considered in this analysis, all rays are meridional and x_p' is zero. Furthermore, since ζ is infinitesimal, the image height may be calculated as

$$y_i'(\zeta, y_p') = M\zeta \tan[u(\zeta, y_p')], \tag{16}$$

where M is the paraxial lateral magnification of the optical system. In addition, the astigmatism term of Eq. (15) is of $O(\zeta^2)$, so this term can be discarded. Using a similar approach, $\eta(\zeta, y_p')$ is found to be equal to

$$\eta(\zeta, y_p') = -n_f L_f \left(\sqrt{1 + (y_p'/L_f)^2} - 1 \right) + W_{040}(y_p')^4. \tag{17}$$

Rearrangement of Eqs. (15)–(17) yields

$$\begin{aligned}
\eta^*(\zeta, y_p') - \eta(\zeta, y_p') &= -n_f L_f \left(\sqrt{1 + \left[y_p'/L_f - y_i'(\zeta, y_p')/L_f\right]^2} - \sqrt{1 + (y_p'/L_f)^2} \right) \\
&\quad + n_f L_f \left(\sqrt{1 + \left[y_i'(\zeta, y_p')/L_f\right]^2} - 1 \right) \\
&\quad + W_{131} M\zeta(y_p')^3 \tan[u(\zeta, y_p')].
\end{aligned} \tag{18}$$

3.4. Solution for marginal ray angle

The wavefront aberration function at the exit pupil is fully-described by Eqs. (14) and (18). However, application of these equations requires expansion of the function for the marginal ray angle $u(\zeta, y_p')$. Since the quantity $u(\zeta, y_p')$ always appears in the form of a product with ζ in Eqs. (14) and (18), any dependence of $u(\zeta, y_p')$ on ζ results in terms of order $O(\zeta^2)$ in the final solution and can be ignored. Consequently, within this specific context the marginal ray angle may be approximated from the initial focus position

$$u(\zeta, y_p') \approx w(y_p'). \tag{19}$$

Within the paraxial approximation, the value of $w(y_p')$ is readily obtained from the Lagrange invariant [57, Eqn. 3.20]

$$w_{\text{paraxial}}(y_p') = -\frac{n_f M y_p'}{n_o L_f}. \tag{20}$$

However, the paraxial approximation cannot be justified here. A third-order relationship may be derived from the Abbe sine condition, but this too makes the undesirable assumption that the initial imaging condition is free of aberrations.

Nonetheless, the required relationship may be obtained by examining the correspondence between coordinates on the entrance and exit pupils. While prior sections examined a ray originating from an on-axis position shifted away from the initial focal plane, the correspondence between the pupils is most easily investigated by following a ray from an off-axis point located on the initial plane. As these are closely related (see Fig. 1(C)), a similar nomenclature is employed. The wavefront aberration function at the entrance pupil for a point on the initial focal plane may be taken as

$$\begin{aligned}
W_e = -n_o L_t \Big(&\sqrt{1 + (x_p/L_t)^2 + (y_p/L_t - y_i/L_t)^2} \\
&- \sqrt{1 + (y_i/L_t)^2} \Big),
\end{aligned} \tag{21}$$

where x_p and y_p are the pupil coordinates, and y_i is the y-coordinate of the off-axis point. The direction cosine of a ray emanating from the entrance pupil is given by

$$\hat{r} \cdot \hat{x} = \frac{1}{n_o} \frac{\partial W_e}{\partial x_p}, \tag{22}$$

where $\hat{r}$ is a unit vector in the direction of the ray at the entrance pupil and $\hat{x}$ is a unit vector in the x-direction. Similarly, the wavefront function at the exit pupil for a point on the initial focal plane may be taken equal to

$$
\begin{aligned}
W_x = -n_f L_f \bigg[&\sqrt{1 + (x_p'/L_f)^2 + (y_p'/L_f - y_i'/L_f)^2} \\
&- \sqrt{1 + (y_i'/L_f)^2} \, \bigg] + W_{040}[(x_p')^2 + (y_p')^2]^2 \\
&+ W_{131} \, y_i' y_p' [(x_p')^2 + (y_p')^2] \\
&+ W_{222} \, (y_i')^2 \, (y_p')^2.
\end{aligned}
\tag{23}
$$

The direction cosine of a ray from the exit pupil is then given by

$$
\hat{r}' \cdot \hat{x} = \frac{1}{n_f} \frac{\partial W_x}{\partial x_p'},
\tag{24}
$$

where $\hat{r}'$ is a unit vector in the direction of the ray. The skew invariant theorem [57, Eqn. 6.23] applies to any axisymmetric system, including those with aberrations, and provides

$$
n_o \, \hat{r} \cdot \hat{x} = n_f \, M \, \hat{r}' \cdot \hat{x},
\tag{25}
$$

where M may again be taken as the paraxial lateral magnification by virtue of the assumption that ζ, and therefore y_i, are infinitesimal.

Since a third-order approximation is required, the correspondence between the entrance and exit pupils is taken as

$$
x_p = A_1 x_p'/L_f + A_2 (x_p'/L_f)^3 + O[(x_p'/L_f)^5],
\tag{26}
$$

where A_1 and A_2 are system dependent constants, and L_f is used to non-dimensionalize the relationships. The values of A_1 and A_2 may be obtained by substituting Eqs. (21)–(24) and Eq. (26) into Eq. (25), further expanding the result as a Taylor series of x_p'/L_f, and then equating the corresponding terms of the resulting polynomial. This yields

$$
A_1 = \frac{n_f M L_t}{n_o}
\tag{27}
$$

$$
A_2 = \frac{(M^2 n_f^3 - n_o^2 n_f - 8 n_o^2 W_{040} L_f^3) M L_t}{2 n_o^3}.
\tag{28}
$$

Since the system is assumed to be axisymmetric, these coefficients also describe the relationship between y_p and y_p' in the presence of third-order aberrations. The relationship between the direction cosine of a ray and the wavefront aberration function gives the angle $w(y_p')$ as

$$
w(y_p') = \arcsin\left(\frac{1}{n_o} \frac{\partial W_e}{\partial y_p} \right).
\tag{29}
$$

Substituting Eqs. (21,26)–(28) into the above and expanding the result as a Taylor series of y_p'/L_f, yields

$$
w(y_p') = -\frac{n_f M}{n_o L_f} y_p' - \frac{(M^2 n_f^3 - 3 n_o^2 n_f - 24 n_o^2 L_f^3 W_{040}) M}{6 n_o^3 L_f^3} (y_p')^3.
\tag{30}
$$

3.5. Closed-form solution for the wavefront function at the exit pupil

The closed-form solution for the wavefront aberration function at the exit pupil may be assembled from the preceding results. Combining Eqs. (14), (18), and (30) and expanding the result as a Taylor series of y_p'/L_f provides

$$
\begin{aligned}
\frac{\partial W_x}{\partial \zeta} = &-\frac{n_f{}^2 M^2}{2 n_o L_f{}^2} (y_p')^2 \\
&- \frac{n_f M^2 (M^2 n_f{}^3 - 4 n_o{}^2 n_f + 8 n_o{}^2 W_{131} L_f{}^3)}{8 n_o{}^3 L_f{}^4} (y_p')^4.
\end{aligned}
\tag{31}
$$

In the above series expansion, the second-order term represents defocus induced by the shift of the focal plane, while the fourth-order term represents spherical aberration. The tuning-induced changes in the wavefront function at the exit pupil differ from those at the entrance pupil (see Eq. (3)) in that they depend on the properties of the intermediate optics. In particular, the induced spherical aberration at the exit pupil varies with the refractive indices of the media at both the object and the exit pupil, the paraxial lateral magnification, the position of the image plane relative to the pupil, and also the coma of the system in the initial configuration.

The contribution of coma to tuning-induced spherical aberration may be understood by consideration of the polynomial order of the relevant terms. Tuning-induced spherical aberration involves a term in the wavefront function of the form $\zeta \times (y_p')^4$. Coma introduces a term of the form $y_i' \times (y_p')^3$ (see Eq. (15)) and y_i' has an approximate form of $\zeta \times y_p'$ (see Eq. (16)), such that coma gives rise to a term of form $\zeta \times (y_p')^4$ similar to a tuning-induced spherical aberration. Alternatively, this may be understood intuitively by recognizing that marginal rays displaced in the axial direction are equivalent to marginal rays emerging from off-axis positions on the initial focal plane, and the path length for these rays is dependent on the coma of the system in the initial configuration (see Fig. 1(C)). Whether coma in the initial configuration also affects tuning-induced coma is unclear, as this falls outside the scope of the present assumptions. However, subsequent sections will further examine the contribution of coma to tuning-induced spherical aberration, and whether the deliberate introduction of coma can be used to null out tuning-induced spherical aberration inherent to tunable lens systems.

3.6. Tracing rays through the tunable lens surface

In order to understand the effects of a tunable lens on spherical aberration, a ray from the exit pupil is next analytically traced through the tunable lens surface. The trajectory of a ray leaving the exit pupil may be calculated from the wavefront aberration function

$$
\begin{aligned}
W_x = &-n_f L_f \left(\sqrt{1 + (y_p'/L_f)^2} - 1 \right) + W_{040}(y_p')^4 \\
&+ \frac{\partial W_x}{\partial \zeta} \zeta(C_t),
\end{aligned}
\tag{32}
$$

where C_t is the curvature of the tunable surface. In expanding this wavefront function, the curvature C_t and and pupil position y_p' are taken as variables, and other quantities are either treated as functions of these values or are fixed properties of the optical system. The angle of a ray relative to the optical axis (see Fig. 2) can be calculated as

$$
\theta_f(C_t, y_p') = \arcsin\left(\frac{1}{n_f} \frac{\partial W_x}{\partial y_p'} \right).
\tag{33}
$$

The variables θ_f and u' represent the same physical quantity, but use different sign conventions to allow for a more intuitive derivation. Expanding Eq. (33) in terms of y_p' yields the Taylor

series

$$\theta_f(C_t, y_p') = F_1(C_t)\left[C_t y_p'\right] + F_2(C_t)\left[C_t y_p'\right]^3,\tag{34}$$

where the pupil height is non-dimensionalized by the surface curvature C_t. The functions $F_1(C_t)$ and $F_2(C_t)$ are constant relative to the pupil position and equal to

$$F_1(C_t) = -\frac{1}{C_t L_f} - \frac{n_f M^2 \zeta(C_t)}{n_o C_t L_f{}^2}\tag{35}$$

$$
\begin{aligned}
F_2(C_t) = \; & \frac{1}{3C_t{}^3 L_f{}^3} + \frac{4W_{040}}{n_f C_t{}^3} \\
& - \frac{M^2(n_f{}^3 M^2 - 3n_o{}^2 n_f + 8L_f{}^3 n_o{}^2 W_{131})\zeta(C_t)}{2n_o{}^3 C_t{}^3 L_f{}^4}.
\end{aligned}\tag{36}
$$
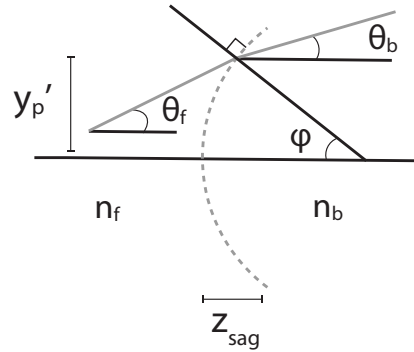
Fig. 2. Schematic diagram of a ray from the exit pupil intercepting the tunable lens surface, indicating quantities used for analytical approximations.

It has been assumed that the tunable lens surface is positioned at the exit pupil, such that the lateral color is unaffected by changes in the tunable lens power. If it is also assumed that the curvature at the lens surface is small and the thin lens approximation applies, then rays intercept the exit pupil and lens surface with the same y-coordinate. Consequently, the angle of the ray at the back of the tunable lens surface may be taken to have a form

$$\theta_b(C_t, y_p') = B_1(C_t)\left[C_t y_p'\right] + B_2(C_t)\left[C_t y_p'\right]^3,\tag{37}$$

where $B_1(C_t)$ and $B_2(C_t)$ are constant relative to the pupil position. These values may be calculated from Snell's Law, which provides

$$n_f \sin\left[\phi(C_t, y_p') + \theta_f(C_t, y_p')\right] - n_b \sin\left[\phi(C_t, y_p') + \theta_b(C_t, y_p')\right] = 0,\tag{38}$$

where n_b is the refractive index of the media behind the tunable surface, and $\phi(C_t, y_p')$ is the angle of the surface normal relative to the optical axis (see Fig. 2). The angle $\phi(C_t, y_p')$ may be calculated from the sag equation for the surface. It is assumed that the surface is approximately spherical and the sag is taken as a fourth order polynomial

$$z_{\text{sag}}(C_t, y_p') = \frac{1}{2}C_t(y_p')^2 + \frac{1}{8}C_t{}^3(y_p')^4 + [\beta + \gamma\zeta(C_t)](y_p')^4,\tag{39}$$

where β is a constant that controls the deviation of the surface from a spherical form, and γ is a constant that represents a tuning-dependent deviation from a spherical form. For a perfectly

spherical surface, β and γ are both zero. The sine and cosine of ϕ may then be calculated as

$$\cos[\phi(C_t, y_p')] = 1/\sqrt{1 + (\partial z_{\text{sag}}/\partial y_p')^2} \tag{40}$$

$$\sin[\phi(C_t, y_p')] = \partial z_{\text{sag}}/\partial y_p'/\sqrt{1 + (\partial z_{\text{sag}}/\partial y_p')^2}. \tag{41}$$

The relationship between the front and back angles may be calculated by expanding Eq. (38), substituting Eqs. (34,40)–(41), expanding the result in terms of a Taylor series of $C_t y_p'$, and equating the coefficients of each of the terms, yielding

$$B_1(C_t) = \frac{n_f - n_b + n_f F_1(C_t)}{n_b} \tag{42}$$

$$
\begin{aligned}
B_2(C_t) = &-\frac{1}{2}[(n_f/n_b)F_1(C_t) - B_1(C_t)] \\
&-\frac{1}{2}\{(n_f/n_b)[F_1(C_t)]^2 - [B_1(C_t)]^2\} \\
&-\frac{1}{6}\{(n_f/n_b)[F_1(C_t)]^3 - [B_1(C_t)]^3\} \\
&+\frac{4(n_f - n_b)}{n_b C_t{}^3}[\beta + \gamma\zeta(C_t)] + (n_f/n_b)F_2(C_t).
\end{aligned}
\tag{43}
$$

3.7. Complete formulae for tuning-induced spherical aberration

If the system is to remain in paraxial focus during tuning, then

$$\frac{\partial}{\partial C_t}\{B_1(C_t)[C_t y_p']\} = 0. \tag{44}$$

Substitution of Eqs. (35), (36), (42), and (43) into Eq. (44) and rearrangement yields the relationship between changes in the surface curvature and the position of the focal plane

$$\frac{\mathrm{d}\zeta}{\mathrm{d}C_t} = -\frac{n_o(n_b - n_f)L_f{}^2}{n_f{}^2 M^2}. \tag{45}$$

Similarly, changes in the surface curvature produce a change in the back angle of

$$\delta S = \frac{\partial \theta_b}{\partial C_t}. \tag{46}$$

Expansion of the above yields a general equation for the tuning induced deviation

$$
\begin{aligned}
\delta S = \frac{(n_b - n_f)(y_p')^3}{2n_o{}^2 n_f{}^2 n_b{}^2 M^2 L_f{}^2}\Big[&n_b n_f{}^4 M^4 - n_o{}^2 n_f M^2(4n_b n_f + n_f{}^2 - 8n_b W_{131} L_f{}^3) \\
&+ 2n_o{}^2 n_f{}^2(n_b + n_f)M^2 C_{to}L_f - n_o{}^2 n_f{}^2(2n_b + n_f)M^2 C_{to}{}^2 L_f{}^2 \\
&+ 8\gamma n_o{}^3 n_b(n_b - n_f)L_f{}^4\Big],
\end{aligned}
\tag{47}
$$

where C_{to} is the initial curvature of the tunable lens surface. It is clear that the tuning-induced spherical aberration is dictated by the refractive indices of the media, the paraxial magnification, the position of the intermediate focal plane relative to the tunable lens surface, the initial lens curvature, coma of the initial system configuration, and any tuning-dependent aspherical form of the tunable surface (prescribed by γ).

Additional insights may be gained by applying some simplifying assumptions. If it is assumed that the tunable lens surface is spherical ($\beta = 0$ and $\gamma = 0$) and has small initial curvature ($C_{to} = 0$), then the solution for δS simplifies to

$$\delta S = \frac{(n_b - n_f)(y_p{}')^3}{2n_o{}^2 n_f n_b{}^2 L_f{}^2}\left[n_b n_f{}^3 M^2 - n_o{}^2(4n_b n_f + n_f{}^2 - 8n_b W_{131}L_f{}^3)\right]. \tag{48}$$

If it is further assumed that the initial imaging system is free of coma, then this deviation goes to zero if and only if the magnification has the value

$$M = \pm\frac{n_o\sqrt{4n_b + n_f}}{n_f\sqrt{n_b}}. \tag{49}$$

This is a powerful result, as it indicates that the tuning-induced spherical aberration may be eliminated simply by designing the system with a real or virtual intermediate image plane at the prescribed magnification just before or after the tunable lens surface.

However, one potential caveat to this approach is that for common optical configurations the prescribed magnification may be smaller than would otherwise be desirable. For example, for a water immersion objective ($n_o = 1.33$, NA=0.8) used with a typical tunable lens material ($n_b = 1.3$ and $n_f = 1.0$), a magnification of ±2.904 is required to produce tuning that does not incur spherical aberration. This magnification also results in a relatively high numerical aperture of 0.275 at the tunable lens surface, which may complicate the system design.

The challenges associated with the prescribed magnification may be relaxed by intentionally introducing coma into the initial optical configuration. By rearranging Eq. (48), it is found that any magnification may be used provided that the coma of the system prior to tunable lens surface is made equal to

$$W_{131} = \frac{n_o{}^2 n_f(4n_b + n_f) - n_b n_f{}^3 M^2}{8n_o{}^2 n_b L_f{}^3}. \tag{50}$$

Critically, coma may be added to the lens elements prior to the tunable surface in order to eliminate tuning-induced spherical aberration, and lens elements after the tunable surface may be used to correct this coma without reintroducing tuning-induced spherical aberration. Using this approach, it is possible to design a complete optical system that is fully corrected in the initial configuration and is simultaneously free from tuning-induced spherical aberration.

In the final case to be examined, it is assumed that the initial imaging system is free of coma and afocal at the tunable lens surface, and tuning-induced spherical aberration is corrected using a tuning-dependent aspheric form. Furthermore, the dimensions of the tunable lens surface are taken to have a paraxial semi-diameter of $h_{max}{}'$ for an angle of u_{max} in the object space. Given these constraints, the position of the image plane is given by

$$L_f = \pm\frac{n_f h_{max}{}'\,|M|}{n_o u_{max}}. \tag{51}$$

Substitution of this relationship into Eq. (47) yields the following requirement for the tuning-dependent aspheric parameter

$$\gamma = -\frac{n_o u_{max}{}^4}{8(n_b - n_f)(h_{max}{}')^4}. \tag{52}$$

4. Conditions for elimination of tuning-induced axial color

Prior studies have examined the axial chromatic aberration of stacks of thin lenses that include tunable surfaces. These studies suggest that multiple tunable surfaces can be used to correct for

tuning-induced axial color [58], but a single tunable surface embedded in an achromatic assembly cannot [35]. This study applies a similar approach but examines the axial color induced by a single tunable surface inside a thick optical system that contains chromatic aberrations in the initial configuration.

The axial chromatic aberration may be calculated by tracing a ray that emerges from an on-axis object that is a distance $L_o + \zeta(C_t)$ from the first principal plane and intersects with a tunable surface located at the exit pupil. The trajectory of this ray is analyzed starting with the ray following refraction from the tunable surface and working backwards toward the object. The relationship between the ray angle following refraction at the tunable surface ($u^\dagger$) and the ray angle prior to the tunable surface (u') may be calculated using the paraxial approximation [57, Eqns. 3.66-67]

$$-n_b(\lambda)\, u^\dagger(C_t, y_p', \lambda) + n_f(\lambda)\, u'(C_t, y_p', \lambda) = -y_p' \left[n_b(\lambda) - n_f(\lambda)\right] C_t, \tag{53}$$

where λ is the wavelength of the light ray, $u^\dagger(C_t, y_p', \lambda)$ is the angle of the ray following refraction, and the other terms are as previously defined, except they are given here as explicit functions of the curvature of the tunable surface and wavelength. The relationship between the ray angle prior to tunable lens (u') and the ray angle at the object (u) is found by observing that the ray emerges from the first principal plane at the same height that it intercepts the second principal plane

$$u'(C_t, y_p', \lambda) \left[L_p + \alpha_2(\lambda)\right] + y_p' = u(C_t, y_p', \lambda) \left[L_o + \zeta(C_t) + \alpha_1(\lambda)\right], \tag{54}$$

where L_p is the distance from the second principal plane to the exit pupil in the initial tuning state for the central wavelength, and $\alpha_1(\lambda)$ and $\alpha_2(\lambda)$ represent wavelength-dependent shifts in the position of the principal planes relative to the physical position of the lens. By continuing to trace the ray backwards, the relationship between the ray angle at the object (u) and the position on the entrance pupil (y_p) is found to be equal to

$$-u(C_t, y_p', \lambda) \left[L_t(\lambda) - \zeta(C_t)\right] = y_p(\lambda). \tag{55}$$

Equations (53)–(55) collectively provide the value of $u^\dagger$ in terms of y_p. To produce a closed-form solution, the position at the entrance pupil (y_p) must be related to the position at the exit pupil (y_p'), which is given by

$$y_p' = M_p(\lambda)\, y_p(\lambda), \tag{56}$$

where $M_p(\lambda)$ is the lateral magnification of the pupil image.

Although Eqs. (53)–(56) describe the desired relationship between $u^\dagger$ and y_p', these equations rely on as yet unknown $\alpha_1(\lambda)$ and $\alpha_2(\lambda)$ functions. Formulae for these quantities may be obtained by observing that for the entrance pupil to image onto the exit pupil [57, Eqn. 3.15], it is necessary that

$$\frac{n_o(\lambda)}{L_t(\lambda) + L_o + \alpha_1(\lambda)} + \frac{n_f(\lambda)}{L_p + \alpha_2(\lambda)} = \frac{1}{f(\lambda)}, \tag{57}$$

where $f(\lambda)$ is the effective focal length of the optical system prior to the tunable surface. Furthermore, the Lagrange invariant [57, Eqn. 3.18] provides that

$$\frac{n_o(\lambda)}{L_t(\lambda) + L_o + \alpha_1(\lambda)} = -\frac{n_f(\lambda)\, M_p(\lambda)}{L_p + \alpha_2(\lambda)}. \tag{58}$$

Equations (57) and (58) may then be solved for $\alpha_1(\lambda)$ and $\alpha_2(\lambda)$. Rearrangement of Eqs. (53)–(58) yields

$$\begin{aligned}
u^\dagger(C_t, y_p', \lambda) = {} & \frac{y_p'}{n_b(\lambda)f(\lambda)M_p(\lambda)} + \frac{[n_b(\lambda) - n_f(\lambda)]C_t y_p'}{n_b(\lambda)} \\
& + \frac{n_o(\lambda)y_p'}{n_b(\lambda)[M_p(\lambda)]^2[L_t(\lambda) - \zeta(C_t)]}.
\end{aligned} \tag{59}$$

Further simplification of Eq. (59) may be achieved by eliminating $\zeta(C_t)$. If the system remains in focus at the central wavelength with changes in tuning,

$$\left. \frac{\partial u^\dagger}{\partial C_t} \right|_{C_{to}, y_p', \lambda_o} = 0, \tag{60}$$

where C_{to} is the curvature of the tunable surface in the initial configuration, and λ_o is the central wavelength. Substitution of Eq. (59) into Eq. (60) and rearrangement yields the following relationship

$$\left. \frac{\mathrm{d}\zeta}{\mathrm{d}C_t} \right|_{C_{to}} = -\frac{[L_t(\lambda_o) M_p(\lambda_o)]^2 [n_b(\lambda_o) - n_f(\lambda_o)]}{n_o(\lambda_o)}. \tag{61}$$

Finally, the tuning-induced axial chromatic aberration may then be taken as the partial derivative of $u^\dagger$ (Eq. (59)) with respect to both C_t and λ, followed by substitution with Eq. (61), yielding

$$
\begin{aligned}
\left. \frac{\partial^2 u^\dagger}{\partial C_t \, \partial \lambda} \right|_{C_{to}, y_p', \lambda_o} &= \frac{y_p' \left[n_b(\lambda_o) - n_f(\lambda_o) \right]}{n_b(\lambda_o)} \left[\frac{2}{M_p(\lambda_o)} \left. \frac{\mathrm{d}M_p}{\mathrm{d}\lambda} \right|_{\lambda_o} - \frac{1}{n_o(\lambda_o)} \left. \frac{\mathrm{d}n_o}{\mathrm{d}\lambda} \right|_{\lambda_o} \right. \\
&\quad \left. + \frac{2}{L_t(\lambda_o)} \left. \frac{\mathrm{d}L_t}{\mathrm{d}\lambda} \right|_{\lambda_o} \right] + \frac{y_p'}{n_b(\lambda_o)} \left[\left. \frac{\mathrm{d}n_b}{\mathrm{d}\lambda} \right|_{\lambda_o} - \left. \frac{\mathrm{d}n_f}{\mathrm{d}\lambda} \right|_{\lambda_o} \right].
\end{aligned} \tag{62}
$$

For certain analyses it may be useful to calculate the tuning-induced axial color in terms of displacements of the focal position rather than changes of the ray angle. The relationship between the two may be found by taking

$$z_b(C_t, \lambda) = \frac{y_p'}{u^\dagger(C_t, y_p', \lambda)}, \tag{63}$$

where $z_b(C_t, \lambda)$ is the virtual focal position formed by rays refracted by the tunable surface. Taking the second-order derivative of Eq. (63) and applying Eq. (60) yields

$$\left. \frac{\partial^2 z_b}{\partial C_t \partial \lambda} \right|_{C_{to}, \lambda_o} = -\frac{[z_b(C_t, \lambda)]^2}{y_p'} \left. \frac{\partial^2 u^\dagger}{\partial C_t \partial \lambda} \right|_{C_{to}, y_p', \lambda_o}. \tag{64}$$

Examination of Eq. (62) reveals that the tuning-induced axial chromatic aberration is zero if the initial configuration meets the following condition

$$\frac{1}{M_p(\lambda_o)} \left. \frac{\mathrm{d}M_p}{\mathrm{d}\lambda} \right|_{\lambda_o} = -\frac{\left. \frac{\mathrm{d}n_b}{\mathrm{d}\lambda} \right|_{\lambda_o} - \left. \frac{\mathrm{d}n_f}{\mathrm{d}\lambda} \right|_{\lambda_o}}{2 \left[n_b(\lambda_o) - n_f(\lambda_o) \right]} + \frac{1}{2 n_o(\lambda)} \left. \frac{\mathrm{d}n_o}{\mathrm{d}\lambda} \right|_{\lambda_o} - \frac{1}{L_t(\lambda)} \left. \frac{\mathrm{d}L_t}{\mathrm{d}\lambda} \right|_{\lambda_o}. \tag{65}$$

This wavelength dependence in the lateral magnification of the pupil represents lateral color of the pupil image. Consequently, this result shows that first-order tuning-induced axial chromatic aberration may be eliminated by introducing lateral color into the pupil image prior to the tunable lens surface. In the general case, this lateral color would also be associated with undesirable tuning-independent axial color in the image space. However, the same strategy used to correct for spherical aberration may be applied here as well. If tuning-induced axial color is absent, then the wavefront emerging from the tunable surface is independent of the tuning state of the system to within the applied approximation level. As a result, after tuning-induced axial color has been eliminated, additional lens elements after the tunable lens may be used to correct for tuning-independent axial color. Using this approach, both the tuning-independent and tuning-induced axial chromatic aberrations may be simultaneously corrected.

5. Numerical verification of analytical predictions

5.1. Simulation of test cases with varying intermediate magnifications

The analytical model developed above indicates that tuning-induced spherical aberration can be eliminated to first-order by designing the system with an intermediate focal plane adjacent to the tunable lens surface with a prescribed magnification. This prediction was examined by evaluating the performance of a series of test cases using exact numerical ray tracing (Zemax OpticStudio 15.5). These designs address a common use case in biological microscopy, axial scanning with a long-working distance, high numerical aperture, water immersion objective. The test system was comprised of a 40x/0.8 water immersion objective, two tube lenses, an air objective that formed an intermediate image plane, a tunable lens surface, and a wavefront reference surface (see Fig. 3(A)). The 40x/0.8 water immersion objective was designed using standard approaches and has diffraction-limited performance over a typical operating range (450-700nm, 22mm field number, 4.4mm working distance; see Fig. 3(B) and Table S1). The two tube lenses had an effective focal length of 200mm and approximate standard Nikon tube lenses (based on published patents [59]; see Table S2). Three air objectives were designed with magnifications of 20x, 13.77x, and 10x using standard approaches (see Fig. 3(D)-I and Tables S3-5). These air objectives produce system magnifications of 4x, 2.904x, and 2x that bracket the value of 2.904x predicted to eliminate first-order tuning-induced spherical aberration for the present conditions ($n_o = 1.33$, $n_f = 1.0$, $n_b = 1.3$). They were each diffraction-limited in conjunction with the water-immersion objective and tube lenses across the full field of view, although since they were designed for test purposes little effort was expended in optimizing them for manufacture. Each of these air objectives was also designed to form a 14mm diameter pupil behind the intermediate image plane, and the tunable lens surface was positioned at this pupil position. The tunable lens surface was taken to have a spherical form that was flat at the initial focal position. A wavefront reference surface was positioned behind the tunable lens, the reference surface was taken as an aspheric surface that zeros the wavefront error across the surface for the initial focal position, such that subsequent measures of wavefront error at this surface reflect tuning-induced aberration. For comparison, the performance was also examined for a system with a traditional design in which the tunable lens surface is positioned at the infinity-focused pupil formed by the tube lenses (Table S6). Tuning-induced wavefront error was assessed similarly, using a reference surface located behind the tunable surface.

For each test case, the object position was varied from -150μm to +150μm along the optical axis, the curvature of the tunable surface was optimized to zero the defocus term of the wavefront function (for λ=497nm), and the spherical aberration term of the wavefront function was computed (9th Zernicke fringe coefficient). As predicted by the analytical model (Eq. (49)), a magnification of 2.904x greatly decreases the effect of focal shift on the spherical aberration term of the wavefront error (Fig. 3(J)). Correspondingly, magnifications above this value (4x, infinite) or below this value (2X) have opposing effects on the first-order tuning-induced spherical aberration. Although tuning-induced spherical aberration is a major contributor to wavefront error, higher-order aberrations are often important in high-NA systems. In order to understand these effects, the Strehl ratio was calculated for each test case as a function of the focal shift (Fig. 3(K)). Since the Strehl ratio includes both lower-order spherical aberration and high-order aberrations, it reflects the overall system performance. The test case with a magnification of 2.904X was found to substantially outperform the other systems examined, achieving a diffraction-limited focal range of 245μm compared to the focal range of 34μm recorded for the traditional infinity-focused configuration.

In order to ensure that the predictions of the analytical model hold under a wide range of conditions, a second test case was also constructed in which n_o, n_f, and n_b were all modified. The configuration of this test case parallels that used above, and consisted of a 40x oil immersion
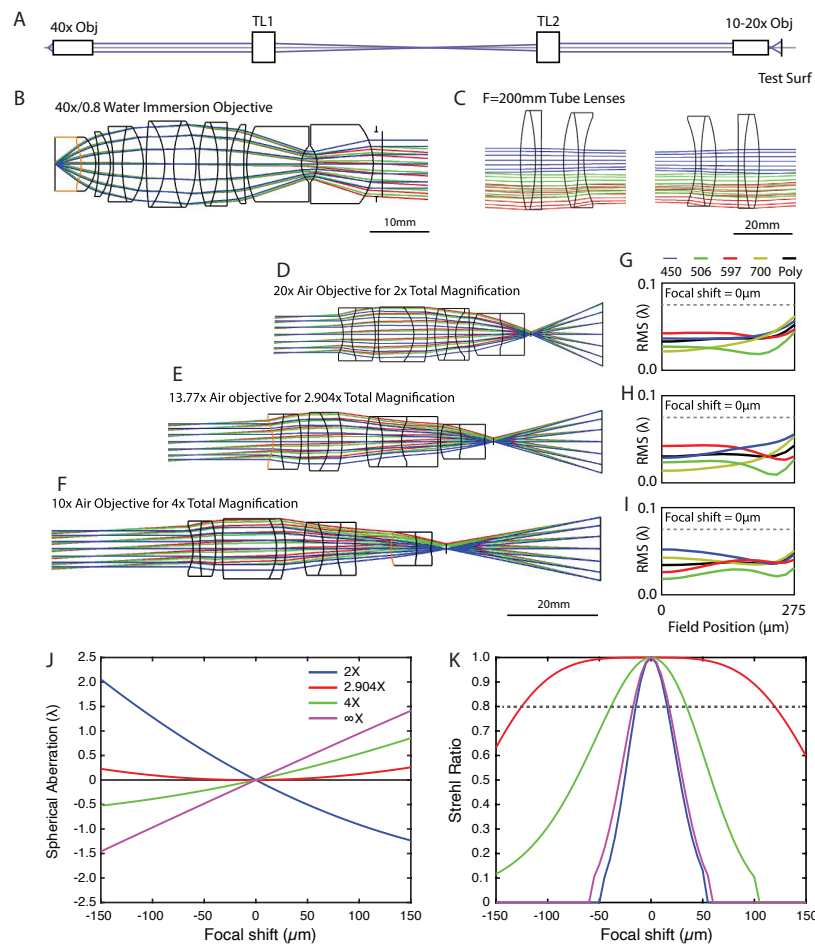
Fig. 3. Tuning-induced spherical aberration of on-axis points is reduced by control of system magnification (A) Schematic diagram of test cases used to examine the effect of system magnification on tuning-induced spherical aberration. (B) A 40x/0.8 water immersion objective designed for the test case. (C) Tube lenses used for the test cases (F=200mm). (D-F) Air objectives with magnifications of 10x, 13.77x, and 20x designed for the test cases. (G-I) RMS wavefront error for objectives in (D-F), respectively, at the initial focus position across the field of view at a range of wavelengths (450nm, 506nm, 597nm, 700nm, polychromatic). The dashed grey line shows an RMS error of 0.075λ, or diffraction-limited performance. (J) The effect of a shift in the focus position on the spherical aberration when a tunable lens surface (n=1.3) is positioned at the pupil to the right of each of the air objectives in (D-F). For each focal position, the curvature of the tunable lens surface was adjusted to hold the system in focus and the spherical aberration was computed at a reference surface positioned behind the tunable lens (λ=497nm). For comparison, the spherical aberration is also shown for a system at infinite magnification (4f system), simulated by omitting the air objective and positioning the tunable surface at the rear pupil. (K) The effect of a shift in the focus position on the Strehl ratio for the test cases of (J) (dashed grey line shows Strehl ratio = 0.8, or diffraction-limited performance).

objective (n_o=1.52), two tube lenses (F=200mm), a water immersion objective that formed an intermediate image (n_f=1.33), a tunable air surface (n_b=1.0), and a wavefront reference surface (see Fig. S1A-C; Table S7-8). The focal length of the water immersion rear objective was optimized to produce an intermediate image with magnifications of 4x, 2.64x, and 2x, centered around the value of 2.64x predicted to eliminate tuning-induced aberration (Eq. (49)). The effect of a focal shift on spherical aberration was examined as above. Consistent with the predictions of the analytical model, the test case with an intermediate magnification of 2.64x displayed little tuning-induced spherical aberration, and magnifications above and below this value showed opposing effects of focal shifts on spherical aberration (Fig. S1D). Similarly, the diffraction-limited focal range of the 2.64x test case was 6-fold greater than that of the 4x test case (Fig. S1E). Residual tuning-induced spherical aberration has a number of potential sources, including wavefront error in the initial configuration, assumptions in the analytical model (e.g., the tunable surface is a thin lens), and other high-order effects. After starting with an initial design based on analytical approximations, it is likely that such residual aberrations may be reduced through subsequent numerical optimization.

5.2. Simulation of test cases with added coma

The results of Section 3.7 suggest that tuning-induced spherical aberration may be reduced by the deliberate introduction of coma into the initial configuration. This prediction was evaluated using numerical ray tracing and the 2x, 2.904x, and 4x test cases described above. In order to ensure that coma was the only property altered, ray tracing was performed from the wavefront described by Eq. (32) through the tunable surface using a custom-written MATLAB script (Mathworks R2020b). Rays were traced from multiple pupil and focal positions (y_p' to 5mm, ζ to 300μm), the curvature of the tunable surface was varied to maintain the system in paraxial focus, and the tuning-induced spherical aberration was characterized by computing $\delta S/(y_p')^3$ (Eq. (46)). The calculated spherical aberration was then evaluated as a function of the coma magnitude W_{131} for each test case and these values were compared to the prediction of the analytical model (Eq. (48)). The results of numerical ray tracing were found to be in very good agreement with the analytical model (Fig. 4). In particular, it was found that when the intermediate image had a magnification of 2.904x tuning-induced spherical aberration was eliminated without added coma ($W_{131} = 0$). When the intermediate image magnification was increased to 4x, the introduction of coma in the amount of $W_{131} = 1.4 \times 10^{-5}\mathrm{mm}^{-3}$ also successfully eliminated tuning-induced spherical aberration. These results suggest that introducing coma into the initial configuration provides a viable approach for correcting tuning-induced spherical aberration.

5.3. Simulation of test cases with an aspherical tunable surface

The analytical model also provides a prediction for the magnitude of the aspheric coefficient necessary to correct for tuning-induced spherical aberrations. This prediction was examined using numerical ray tracing and test cases mirroring those used above for examining the effects of system magnification. The test system consisted of a 40x water immersion objective, two F=200mm tube lenses, and a tunable aspherical lens surface (n=1.3, spherical + 4th-order polynomial) positioned at the rear pupil. A flat wavefront reference surface was positioned behind the tunable lens. The object position was then varied from -150μm to +150μm along the optical axis, and the parameters for the tunable surface were optimized to zero the defocus and spherical aberration terms of the wavefront function (for λ=497nm). This calculation was performed for a lens system operating at reduced aperture (NA=0.2) and at full aperture (NA=0.8), and the computed 4th-order aspheric coefficients were examined as a function of the focal shift. The 4th-order coefficients computed using this approach were found to vary in an approximately linear manner with the focal shift (Fig. 5(A)). The reduced aperture (NA=0.2) test case and analytical model produced nearly identical results over the examined focal shift, which strongly supports
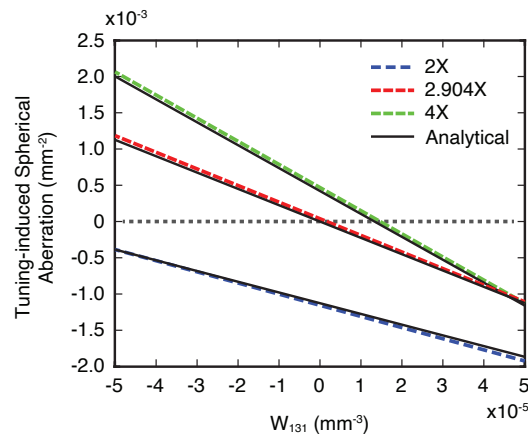
Fig. 4. Tuning-induced spherical aberration is reduced by added coma The effect of added coma (W_{131}) on the tuning-induced spherical aberration ($\delta S/(y_p')^3$), calculated using numerical ray tracing and analytical modeling (Eq. (48)). Simulations were performed for the 2x, 2.904x, and 4x test cases described in Fig. 3 (λ=497nm).

the correctness of the analytical model. The full aperture (NA=0.8) test case yielded coefficients that were 44% greater for this particular system, likely reflecting the influence of higher-order aberrations that had less weight in the smaller aperture test case and were neglected in the analytical model. In order to understand the practical effects of these reductions in aberration, the Strehl ratio was also computed as a function of the focal shift, and the aspheric tunable surface was found to allow for diffraction-limited performance over the entire 300μm that was examined (Fig. 5(B)).

Given the favorable performance observed for on-axis points, the widefield performance of a system incorporating an aspherical tunable surface was next examined. The test case described above was modified, optimizing the RMS wavefront error across the design field of view (550μm) by varying the curvature and 4th order aspheric coefficient for each focal position. The Strehl ratio for points at the edge of the field of view was then calculated for each focal position. Despite the promising performance of the on-axis system, the Strehl ratio for an off-axis point was found to deteriorate quickly as the focal position was shifted (Fig. 5(C)). Next, this test case was re-optimized for polychromatic light (450-650nm), and the Strehl ratio at an off-axis point was computed for a central wavelength (497nm) as a function of the focal position. As might be expected, the inclusion of chromatic aberrations resulted in further decreases of the Strehl ratio and additional narrowing of the diffraction-limited focal shift range.

5.4. Simulation of test cases with reduced tuning-induced axial color

The analytical modeling of Section 4 predicts that first-order tuning-induced axial color can be eliminated by introducing lateral color into the pupil image. That prediction was evaluated with numerical ray tracing and a test system that parallels the one used above to examine the effects of magnification on tuning-induced spherical aberration. This system included a 40x water immersion objective, two F=200mm tube lenses, a 13.77x air objective, a spherical tunable lens surface (n=1.3), and an aspherical wavefront reference surface positioned behind the tunable lens. A larger than typical Abbe number was used for the tunable lens surface (v_d=30) to increase the axial chromatic aberration and provide a stricter test. The simulations were implemented with a multi-configurational system that examined a central and offset wavelength (λ=497nm and 597nm) as well as image formation with the initial focus position, image formation at a displaced
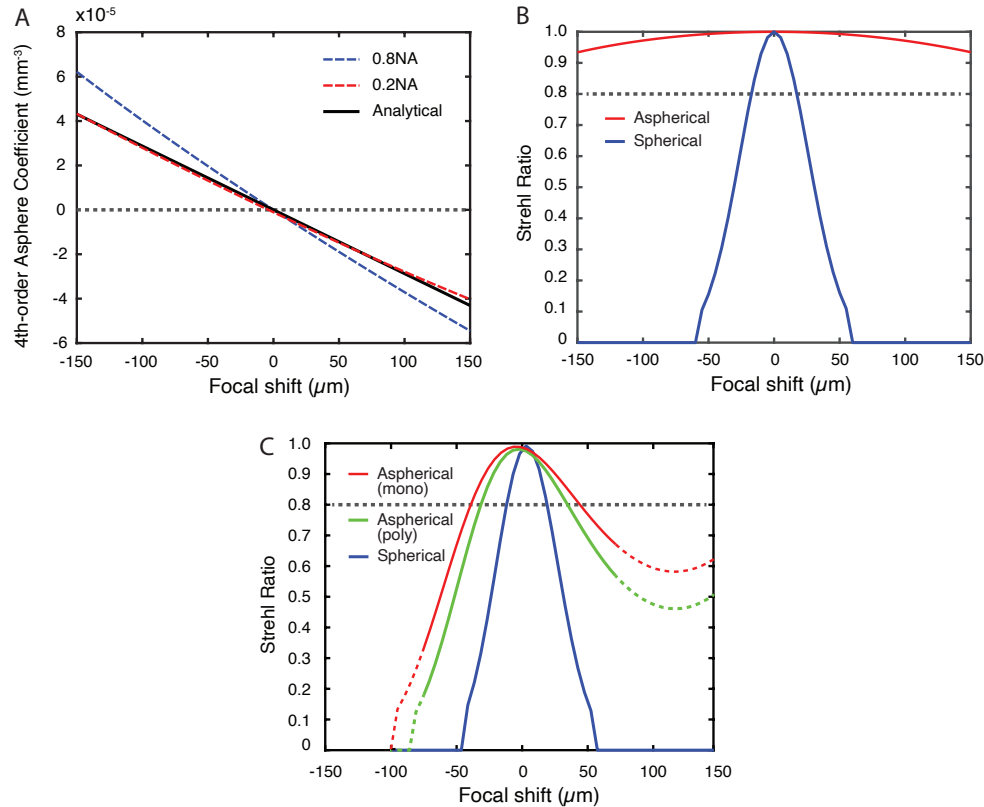
Fig. 5. Tuning-induced aberration is reduced with an aspherical tunable surface (A) The effect of focal shift on the optimal 4th-order aspheric coefficient. An aspherical tunable lens surface (n=1.3, spherical + 4th-order) was positioned at the rear pupil of the infinite magnification system of Fig. 3, and the curvature and 4th-order aspheric coefficient were optimized to minimize wavefront error for an on-axis ray pencil (λ=497nm) on a reference surface behind the tunable lens. Three solutions are shown: optimization for a large-angle 0.8NA object pencil, optimization for an intermediate-angle 0.2NA ray pencil, and the analytical solution provided in Eq. (52). (B) Strehl ratio for the aspherical system of (A) (red), compared against a similar system with a spherical tunable surface (blue) (dashed grey line shows Strehl ratio = 0.8, or diffraction-limited performance). (C) Strehl ratio at the edge of the field of view for a system similar to that of (A) (λ=497nm). The system was optimized to reduce the RMS wavefront error across the entire field of view for monochromatic light (λ=497nm; red) and polychromatic light (497nm; green). The dashed grey line shows Strehl ratio = 0.8, and the dashed parts of the data curves show regions where vignetting is unavoidable with the stock tube lens design.

focus position (ζ=300μm), and pupil image formation. The system was then modified to vary the pupil lateral color ($1/M_p\, dM_p/d\lambda$) by optimizing the radii and spacing of the tube lens and air objective surfaces. Since there are a large number of free variables, a strict comparison requires the system to be carefully constrained to match the assumptions of the analytical model. The applied constraints included that the intermediate image in front of the tunable lens is free of monochromatic aberrations at the central wavelength and has a fixed magnification (2.904x), the curvature of the tunable surface eliminates the defocus term of the wavefront error, the exit pupil is located at the tunable surface and has no axial color, and the reference surface is updated so that the wavefront error remains zero at the initial focus position for the central wavelength.

Using the above test case, the tuning-induced axial color was calculated as the difference in the chromatic focal shift between the displaced (ζ=300μm) and initial (ζ=0μm) states, and this value was compared to that predicted by the analytical model (Eq. (63)). The results of the numerical simulations and analytical model were found to be in excellent agreement, and demonstrate that the deliberate introduction of lateral color into the pupil image can be used to remove tuning-induced axial color (Fig. 6). Finally, although a rigorous numerical approach was employed here, for typical design efforts it is likely that a simple constraint on the lateral pupil color is sufficient to yield color-corrected systems.
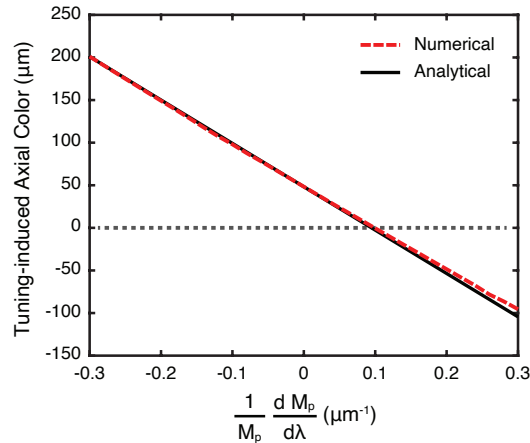

Fig. 6. Tuning-induced axial color is reduced by controlling lateral pupil color. The effect of varying the lateral color of the pupil image on the tuning-induced axial color for a test case based on the 2.904x system of Fig. 3. Results are shown for numerical ray tracing (dashed red line) and the analytical solution (black line) provided in Eq. (63).

6. Design of a widefield axial-scanning optical system

In order to explore how these findings may be practically applied, the identified conditions were used to guide the design of a 40x axial-scanning microscope system. This system was comprised of a 40x water immersion objective, two tube lenses, an air objective, a commercially available tunable lens element (Optotune EL-16-40-TC), and a relay lens. The first design iteration was based upon the 2.904x test case described above, thereby eliminating tuning-induced spherical aberration at a central wavelength. Multi-configurational optimization was then used to further refine this design and improve the imaging quality for off-axis points. This optimization was constrained such that the first tube lens formed a diffraction-limited intermediate image for the initial configuration, as this is likely to ease the integration of such a system into a modular microscope system. During axial scanning the intermediate image formed between the tube

lenses shifts forward and backward. The optimization was further constrained such that this intermediate image does not pass into either tube lens, so that dust and surface imperfections on these lens surfaces do not produce artifacts in the final image. In addition, the optimization was constrained to produce a system pupil between tube lens 2 and the air objective. Although this pupil remains empty in this design, a deformable mirror adaptive optics element could be easily integrated at this position in order to compensate for small wavefront aberrations that may be introduced by the sample object or from imperfections in the tunable lens. Lastly, the system was constrained to avoid vignetting for any field or focal position, and to use only viable tunable lens powers (lens is specified for -10 dpt to 10 dpt, optimized design uses 5.07 to 8.43 dpt range).

This process yielded a design with a wide field of view (550 µm), large focal shift range (350 µm), large numerical aperture (NA=0.8), wide wavelength range (apochromatic correction, 450-625nm), constant magnification, and diffraction-limited performance across the operating
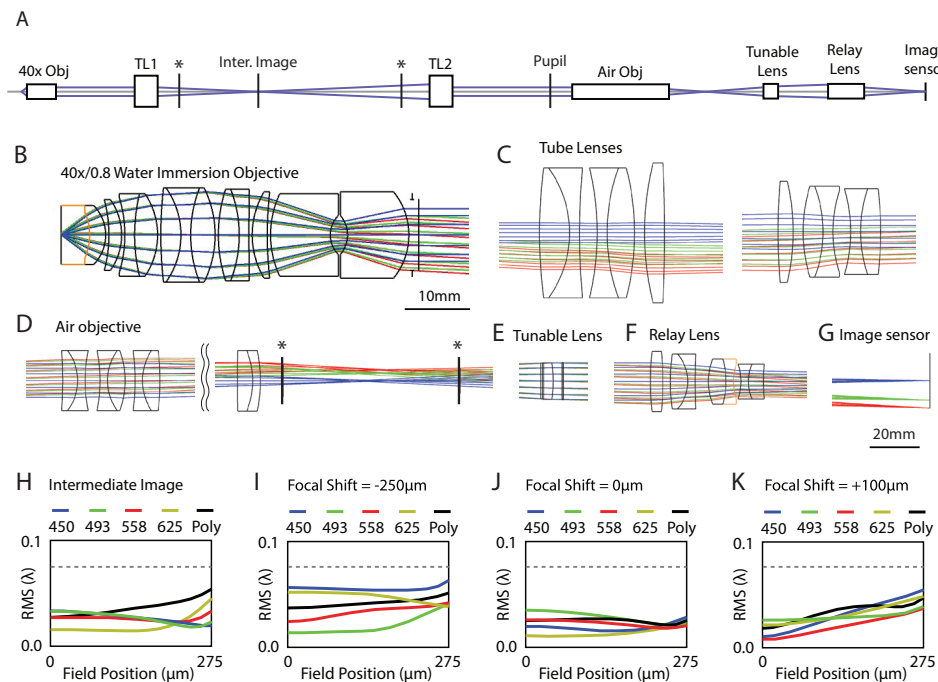

Fig. 7. Design of diffraction-limited, wide-field, axial-scanning 40x microscope system
(A) Schematic diagram of the optical path, comprising a 40x water immersion objective, two tube lenses (TL1 and TL2), an air objective, a tunable lens, a relay lens, and an image sensor. The positions of the following are indicated: the intermediate image formed between TL1 and TL2 for an object at the design focal position of the objective ("inter. image"), the intermediate images formed for objects shifted by -250µm and +100µm (planes with asterisks), and a pupil in front of the air objective. (B) A 40x/0.8 water immersion objective (same as Fig. 3(B)). (C) Designed tube lenses. (D) Designed air objective. (E) Model of commercially-available tunable lens (Optotune EL-16-40-TC). (F) Designed relay lens. (G) Rays at the image sensor (C-G drawn at same scale). (H) RMS wavefront error at the intermediate image for an object at the design focal position of the objective (dashed grey line shows RMS error of 0.075λ or diffraction-limited performance). (I-K) RMS wavefront error at the image sensor for objects shifted by -250µm, 0µm, and +100µm (dashed grey line shows RMS error of 0.075λ).

range (Fig. 7; Table S9). The achieved focal shift range (350 µm) is approximately an order of magnitude greater than the diffraction-limited range of a traditional infinity-focused design (34µm; Fig. 3(K)). The design produces an intermediate image before the tunable lens that has a lower magnification (15.2x) than would be expected if this intermediate image was aberration-free (Eq. (47)). However, this intermediate image contains a substantial amount of coma, which has been shown to assist in eliminating tuning-induced spherical aberration (Eq. (50)). This coma and other aberrations present in the initial configuration are corrected by the relay lens behind the tunable surface, such that both the tuning-independent and tuning-induced aberrations are simultaneously corrected. This system was designed to be very highly corrected across the operating range ($<0.06\lambda$ polychromatic RMS wavefront error) in order to demonstrate the feasibility of such correction, but it may be reasonable for future designs to sacrifice some performance to reduce costs.

7. Discussion

This study examines the spherical and chromatic aberrations of axial-scanning optical systems containing a tunable lens element, with a particular emphasis on high numerical aperture configurations that are common for biological microscopy. It is shown that tuning-induced spherical aberration for on-axis points can be eliminated by controlling the lateral magnification and coma of the optics prior to the tunable surface. Consistent with prior experimental studies [50–52], it is also found that a tuning-dependent aspherical surface can be used to reduce aberrations for on-axis points and, to a more limited extent, off-axis points. Furthermore, it is shown that tuning-induced axial chromatic aberration may be eliminated by introducing lateral color of the pupil image prior to the tunable surface. The conditions necessary to eliminate tuning-induced lateral color, changes in magnification, spherical aberration, and axial color are described with simple formulae appropriate for design purposes. These insights are then used to design a high-NA axial-scanning microscopy system that provides diffraction limited performance over a wide field of view (550µm) and deep axial range (350µm).

Tunable optical elements provide an effective means of performing rapid axial scanning, and the results presented here demonstrate that tuning-induced aberrations may be eliminated through system-level design. Although the analytical approximations developed in this manuscript focus on lower-order aberrations, higher-order aberrations often play a significant role in the total wavefront error for high-NA systems. The presented design of a high-NA axial-scanning system (Fig. 7) demonstrates that if lower-order aberrations are eliminated with analytical constraints that high-order aberrations may be corrected through numerical optimization. In addition, the analytical approaches applied in this study could be extended to capture higher order terms if additional insights into these terms were necessary. A potential caveat to these findings is that it is unclear if current tunable lenses provide the high surface accuracy necessary for diffraction-limited performance over wide focus ranges. However, rapid progress in lens manufacturing techniques suggests that surface accuracy will continue to improve [43,45–52]. Furthermore, the present analysis shows that unintentional deviations from a spherical form can be mitigated by adjusting the design of other optical components (Eq. (47)), provided the deviations are consistent and known [37]. Consequently, high-performance tunable lens systems appear poised to drive major advances in volumetric imaging and biological microscopy.

Supplemental document. See Supplement 1 for supporting content.

References

1. M. Minsky, "Microscopy apparatus," US Patent **US3013467A**, (1961).

2. C. J. R. Sheppard and A. Choudhury, "Image Formation in the Scanning Microscope," Opt. Acta **24**(10), 1051–1073 (1977).

3. W. Denk, J. H. Strickler, and W. W. Webb, "Two-photon laser scanning fluorescence microscopy," Science **248**(4951), 73–76 (1990).

4. P. J. Keller, A. D. Schmidt, J. Wittbrodt, and E. H. K. Stelzer, "Reconstruction of Zebrafish Early Embryonic Development by Scanned Light Sheet Microscopy," Science **322**(5904), 1065–1069 (2008).

5. R. Tomer, K. Khairy, F. Amat, and P. J. Keller, "Quantitative high-speed imaging of entire developing embryos with simultaneous multiview light-sheet microscopy," Nat. Methods **9**(7), 755–763 (2012).

6. K.-S. Lee, P. Vanderwall, and J. P. Rolland, "Two-photon microscopy with dynamic focusing objective using a liquid lens," in *Multiphoton Microscopy in the Biomedical Sciences X*, vol. 7569 (International Society for Optics and Photonics, 2010), p. 756923.

7. B. F. Grewe, F. F. Voigt, M. van 't Hoff, and F. Helmchen, "Fast two-layer two-photon imaging of neuronal cell populations using an electrically tunable lens," Biomed. Opt. Express **2**(7), 2035–2046 (2011).

8. F. O. Fahrbach, F. F. Voigt, B. Schmid, F. Helmchen, and J. Huisken, "Rapid 3D light-sheet microscopy with a tunable lens," Opt. Express **21**(18), 21010–21026 (2013).

9. J. M. Jabbour, B. H. Malik, C. Olsovsky, R. Cuenca, S. Cheng, J. A. Jo, Y.-S. L. Cheng, J. M. Wright, and K. C. Maitland, "Optical axial scanning in confocal microscopy using an electrically tunable lens," Biomed. Opt. Express **5**(2), 645–652 (2014).

10. T. Hinsdale, B. H. Malik, C. Olsovsky, J. A. Jo, and K. C. Maitland, "Volumetric structured illumination microscopy enabled by a tunable-focus lens," Opt. Lett. **40**(21), 4943–4946 (2015).

11. K. Philipp, A. Smolarski, N. Koukourakis, A. Fischer, M. Stürmer, U. Wallrabe, and J. W. Czarske, "Volumetric HiLo microscopy employing an electrically tunable lens," Opt. Express **24**(13), 15029–15041 (2016).

12. M. Duocastella, G. Sancataldo, P. Saggau, P. Ramoino, P. Bianchini, and A. Diaspro, "Fast inertia-free volumetric light-sheet microscope," ACS Photonics **4**(7), 1797–1804 (2017).

13. K.-J. Hsu, K.-Y. Li, Y.-Y. Lin, A.-S. Chiang, and S.-W. Chu, "Optimizing depth-of-field extension in optical sectioning microscopy techniques using a fast focus-tunable lens," Opt. Express **25**(14), 16783–16794 (2017).

14. C. Chong, L. Simin, W. Gang, L. Yong, W. Linbo, Y. Guang, J. Xin, and L. Hui, "Four-dimensional visualization of zebrafish cardiovascular and vessel dynamics by a structured illumination microscope with electrically tunable lens," Biomed. Opt. Express **11**(2), 1203–1215 (2020).

15. E. J. Botcherby, R. Juskaitis, M. J. Booth, and T. Wilson, "Aberration-free optical refocusing in high numerical aperture microscopy," Opt. Lett. **32**(14), 2007–2009 (2007).

16. E. J. Botcherby, C. W. Smith, M. M. Kohl, D. Debarre, M. J. Booth, R. Juskaitis, O. Paulsen, and T. Wilson, "Aberration-free three-dimensional multiphoton imaging of neuronal activity at kHz rates," Proc. Natl. Acad. Sci. U. S. A. **109**(8), 2919–2924 (2012).

17. E. J. Botcherby, R. Juškaitis, and T. Wilson, "Scanning two photon fluorescence microscopy with extended depth of field," Opt. Commun. **268**(2), 253–260 (2006).

18. G. Thériault, Y. D. Koninck, and N. McCarthy, "Extended depth of field microscopy for rapid volumetric two-photon imaging," Opt. Express **21**(8), 10095–10104 (2013).

19. A. Song, A. S. Charles, S. A. Koay, J. L. Gauthier, S. Y. Thiberge, J. W. Pillow, and D. W. Tank, "Volumetric two-photon imaging of neurons using stereoscopy (vTwINS)," Nat. Methods **14**(4), 420–426 (2017).

20. S. K. Jericho, M. H. Jericho, and H. J. Kreuzer, "Digital in-line holographic microscopy in 4-D," in *Biomedical Optics and 3-D Imaging (2010), paper DTuA1* (Optical Society of America, 2010), p. DTuA1.

21. H. Ren, D. Fox, P. A. Anderson, B. Wu, and S.-T. Wu, "Tunable-focus liquid lens controlled using a servo motor," Opt. Express **14**(18), 8031–8036 (2006).

22. H. Ren, H. Xianyu, S. Xu, and S.-T. Wu, "Adaptive dielectric liquid lens," Opt. Express **16**(19), 14954–14960 (2008).

23. L. Miccio, M. Paturzo, S. Grilli, V. Vespini, and P. Ferraro, "Hemicylindrical and toroidal liquid microlens formed by pyro-electro-wetting," Opt. Lett. **34**(7), 1075–1077 (2009).

24. L. Li, J.-H. Wang, Q.-H. Wang, and S.-T. Wu, "Displaceable and focus-tunable electrowetting optofluidic lens," Opt. Express **26**(20), 25839–25848 (2018).

25. J. Kim, J. Kim, J.-H. Na, B. Lee, and S.-D. Lee, "Liquid crystal-based square lens array with tunable focal length," Opt. Express **22**(3), 3316–3324 (2014).

26. T. Inagaki, T. Imai, J. Miyazu, and J. Kobayashi, "Polarization independent varifocal lens using KTN crystals," Opt. Lett. **38**(15), 2673–2675 (2013).

27. M. Duocastella, G. Vicidomini, and A. Diaspro, "Simultaneous multiplane confocal microscopy using acoustic tunable lenses," Opt. Express **22**(16), 19293–19301 (2014).

28. S. Piazza, P. Bianchini, C. Sheppard, A. Diaspro, and M. Duocastella, "Enhanced volumetric imaging in 2-photon microscopy via acoustic lens beam shaping," J. Biophotonics **11**, (2018).

29. Y. Yasuno, S. Makita, T. Yatagai, T. Wiesendanger, A. Ruprecht, and H. Tiziani, "Non-mechanically-axial-scanning confocal microscope using adaptive mirror switching," Opt. Express **11**(1), 54–60 (2003).

30. W. J. Shain, N. A. Vickers, B. B. Goldberg, T. Bifano, and J. Mertz, "Extended depth-of-field microscopy with a high-speed deformable mirror," Opt. Lett. **42**(5), 995–998 (2017).

31. S. Kang, M. Duocastella, and C. B. Arnold, "Variable optical elements for fast focus control," Nat. Photonics **14**(9), 533–542 (2020).

32. A. Miks and J. Novák, "Third-order aberrations of the thin refractive tunable-focus lens," Opt. Lett. **35**(7), 1031–1033 (2010).

33. S. Murali, P. Meemon, K.-S. Lee, W. P. Kuhn, K. P. Thompson, and J. P. Rolland, "Assessment of a liquid lens enabled in vivo optical coherence microscope," Appl. Opt. **49**(16), D145–156 (2010).

34. N. Koukourakis, M. Finkeldey, M. Stürmer, C. Leithold, N. C. Gerhardt, M. R. Hofmann, U. Wallrabe, J. W. Czarske, and A. Fischer, "Axial scanning in confocal microscopy employing adaptive lenses (CAL)," Opt. Express **22**(5), 6025–6039 (2014).

35. Y. Yan, X. Tian, R. Liang, and J. Sasian, "Optical performance evaluation and chromatic aberration correction of a focus tunable lens used for 3D microscopy," Biomed. Opt. Express **10**(12), 6029–6042 (2019).

36. Y.-K. Fuh, K.-C. Hsu, M.-X. Lin, and J.-R. Fan, "Adjustable fluidic lenses for correcting piston/defocus/astigmatism aberrations induced by MEMS deformable mirrors," Microw. Opt. Technol. Lett. **54**(7), 1701–1705 (2012).

37. Y.-K. Fuh, J.-K. Chen, and P.-W. Chen, "Characterization of electrically tunable liquid lens and adaptive optics for aberration correction," Optik **126**(24), 5456–5459 (2015).

38. S. Reichelt and H. Zappe, "Design of spherically corrected, achromatic variable-focus liquid lenses," Opt. Express **15**(21), 14146–14154 (2007).

39. Y.-C. Fang and C.-M. Tsai, "Miniature lens design and optimization with liquid lens element via genetic algorithm," J. Opt. A: Pure Appl. Opt. **10**(7), 075304 (2008).

40. A. Miks, J. Novak, and P. Novak, "Generalized refractive tunable-focus lens and its imaging characteristics," Opt. Express **18**(9), 9034–9047 (2010).

41. L. Li and Q.-H. Wang, "Zoom lens design using liquid lenses for achromatic and spherical aberration corrected target," Opt. Eng. **51**(4), 043001 (2012).

42. L. Li, D. Wang, C. Liu, and Q.-H. Wang, "Zoom microscope objective using electrowetting lenses," Opt. Express **24**(3), 2931–2940 (2016).

43. H. Yu, G. Zhou, H. M. Leung, and F. S. Chau, "Tunable liquid-filled lens integrated with aspherical surface for spherical aberration compensation," Opt. Express **18**(10), 9945–9954 (2010).

44. A. Miks, J. Novak, and P. Novak, "Algebraic and numerical analysis of imaging properties of thin tunable-focus fluidic membrane lenses with parabolic surfaces," Appl. Opt. **52**(10), 2136–2144 (2013).

45. K. Mishra, C. Murade, B. Carreel, I. Roghair, J. M. Oh, G. Manukyan, D. van den Ende, and F. Mugele, "Optofluidic lens with tunable focal length and asphericity," Sci. Rep. **4**(1), 6378 (2015).

46. M. C. Wapler, M. Stürmer, and U. Wallrabe, "A compact, large-aperture tunable lens with adaptive spherical correction," in *2014 International Symposium on Optomechatronic Technologies* (2014), pp. 130–133.

47. P. Zhao, C. Ataman, and H. Zappe, "Spherical aberration free liquid-filled tunable lens with variable thickness membrane," Opt. Express **23**(16), 21264–21278 (2015).

48. Y.-K. Fuh and P.-W. Chen, "Novel dual-function lens with microscopic and vari-focus capability incorporated with an aberration-suppression aspheric lens," Opt. Express **23**(17), 21771–21785 (2015).

49. K. Wei, H. Huang, Q. Wang, and Y. Zhao, "Focus-tunable liquid lens with an aspherical membrane for improved central and peripheral resolutions at high diopters," Opt. Express **24**(4), 3929–3939 (2016).

50. K. Philipp, F. Lemke, S. Scholz, U. Wallrabe, M. C. Wapler, N. Koukourakis, and J. W. Czarske, "Diffraction-limited axial scanning in thick biological tissue with an aberration-correcting adaptive lens," Sci. Rep. **9**(1), 9532 (2019).

51. H. Zhou, X. Zhang, Z. Xu, P. Wu, and H. Yu, "Universal membrane-based tunable liquid lens design for dynamically correcting spherical aberration over user-defined focal length range," Opt. Express **27**(26), 37667–37679 (2019).

52. M. C. Wapler, "Ultra-fast, high-quality and highly compact varifocal lens with spherical aberration correction and low power consumption," Opt. Express **28**(4), 4973–4987 (2020).

53. S. Murali, K. P. Thompson, and J. P. Rolland, "Three-dimensional adaptive microscopy using embedded liquid lens," Opt. Lett. **34**(2), 145–147 (2009).

54. S. Liu and H. Hua, "Extended depth-of-field microscopic imaging with a variable focus microscope objective," Opt. Express **19**(1), 353–362 (2011).

55. G. Lan, T. F. Mauger, and G. Li, "Design of high-performance adaptive objective lens with large optical depth scanning range for ultrabroad near infrared microscopic imaging," Biomed. Opt. Express **6**(9), 3362–3377 (2015).

56. M. Martinez-Corral, P.-Y. Hsieh, A. Doblas, E. Sanchez-Ortiga, G. Saavedra, and Y.-P. Huang, "Fast Axial-Scanning Widefield Microscopy With Constant Magnification and Resolution," J. Disp. Technol. **11**(11), 913–920 (2015).

57. W. Welford, *Aberrations of Optical S+ystems* (Taylor & Francis, 1986).

58. P. Novak, J. Novak, and A. Miks, "Analysis and application of refractive variable-focus lenses in optical microscopy," in *Modeling Aspects in Optical Metrology III*, vol. 8083 (International Society for Optics and Photonics, 2011), p. 808316.

59. M. Mandai and K. Yamaguchi, "Immersion microscope objective lens," US Patent **US7046451B2**, (2006).